CHEMISTRY OF MATERIALS

Platinum Selenide Nanoparticle Synthesis and Reaction with Butyllithium Breaking the Long-Range Ordering Structure

Victor Secco Lemos, Daniel Angeli de Moraes, Iara de Lacerda Pataca, Olavo Fiamencini Verruma, Carolina Pirogini Torres, Angela Albuquerque, Ingrid Rodríguez-Gutiérrez, Danilo Biazon Janes, Felipe Crasto de Lima, Flavio Leandro Souza, Edson Roberto Leite, Adalberto Fazzio, and João Batista Souza Junior*

Cite This: *Chem. Mater.* 2024, 36, 8613−8622

Read Online

ACCESS | Metrics & More | Article Recommendations | Supporting Information

ABSTRACT: $PtSe_2$ is a transition metal dichalcogenide (TMD) material with a broad range of applications, such as sensors, electronics, and catalysis. Although 2D monolayers of $PtSe_2$ have been widely studied, the synthesis of controlled $PtSe_2$ nanoparticles (NPs) is still unexplored. Here, the new strategy to synthesize $PtSe_2$ NPs was to react Pt NPs with selenium in a liquid state inside a homemade closed reactor. Afterward, the $PtSe_2$ NPs reaction with butyllithium led to cleavage of the covalent bond along the *ab*-plane of 2D material (intralayer) and broke the $PtSe_2$ long-range structure. The result was a $PtSe_x$ nanomaterial with a greater concentration of defects having only the short-range ordering but keeping the local structure, as proved by Raman and ePDF analyses. X-ray photoelectron spectroscopy revealed a higher contribution from defects (Pt 4f ~72 eV) for $PtSe_x$ compared to the crystalline $PtSe_2$ chemical environment (~73.2 eV), probably due to the creation of edges on the surface of $PtSe_x$. $PtSe_2$, and $PtSe_x$ NPs' performance toward the hydrogen evolution reaction (HER) application was tested, which indicated a better efficiency than bulk $PtSe_2$. However, the disordered $PtSe_x$ sample has better electrocatalytic activity, as the number of defects and increased edge exposure create more active sites. Therefore, the results reported here indicate that $PtSe_2$ NPs can be produced using a fast and simple method compared to standard selenization processes, and the activation toward the HER was further enhanced by defect engineering.

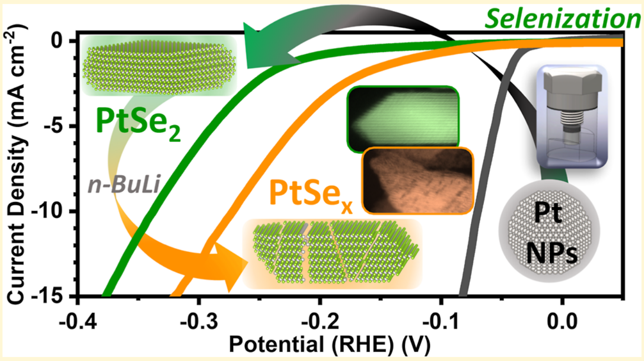

INTRODUCTION

In the past decades, the ability to synthesize nanomaterials and explore their unique properties has evolved to control nanomaterials' morphology, achieving new or exciting phenomena.[1] Within the universe of controlled nanomaterials, 2D materials could be pointed out as one of the most promising alternatives for high-end electronics, spintronics, optoelectronics, energy harvesting, flexible electronics, etc.[2−4] Transition metal dichalcogenides (TMDs) are semiconducting materials with the general formula MX_2, with M being a transition metal atom and X a chalcogen atom (S, Se, or Te). TMDs have a distinctive layered structure with strong covalent bonds within the monolayers and weak van der Waals (vdW) interactions between layers, making them an excellent platform for developing 2D structures for these applications.[2] Although the TMDs include several different materials with unique properties based on their phase structure and chemical composition,[5,6] the group-6 TMDs with 2H (semiconducting) phases, such as MoS_2 and WSe_2, have been subject to intense studies in the recent literature due to their robustness.[7−10] According to theoretical predictions, group-10 TMDs (e.g., $PtSe_2$ and PtS_2) may also be highly desirable materials for photocatalytic, hydrogen evolution,[11] and optoelectronic devices.[8] Recent studies have also identified these materials as candidates for exotic electronic structures, presenting quantum topological properties. This property allows insulating behavior in the bulk while possessing metallic surface states when defects are induced.[12−14] Regarding TMD's energy application for hydrogen evolution reaction (HER), the basal plane sites are less active for electrocatalytic reactions compared to edges and defects serving as additional important catalytic sites.[15] 2D TMDs, which expose mostly the inactive basal plane, have been extensively investigated for HER, but there have been only a few reports on TMD nanoparticles

Received: March 13, 2024
Revised: August 28, 2024
Accepted: August 29, 2024
Published: September 10, 2024

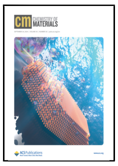

https://doi.org/10.1021/acs.chemmater.4c00753

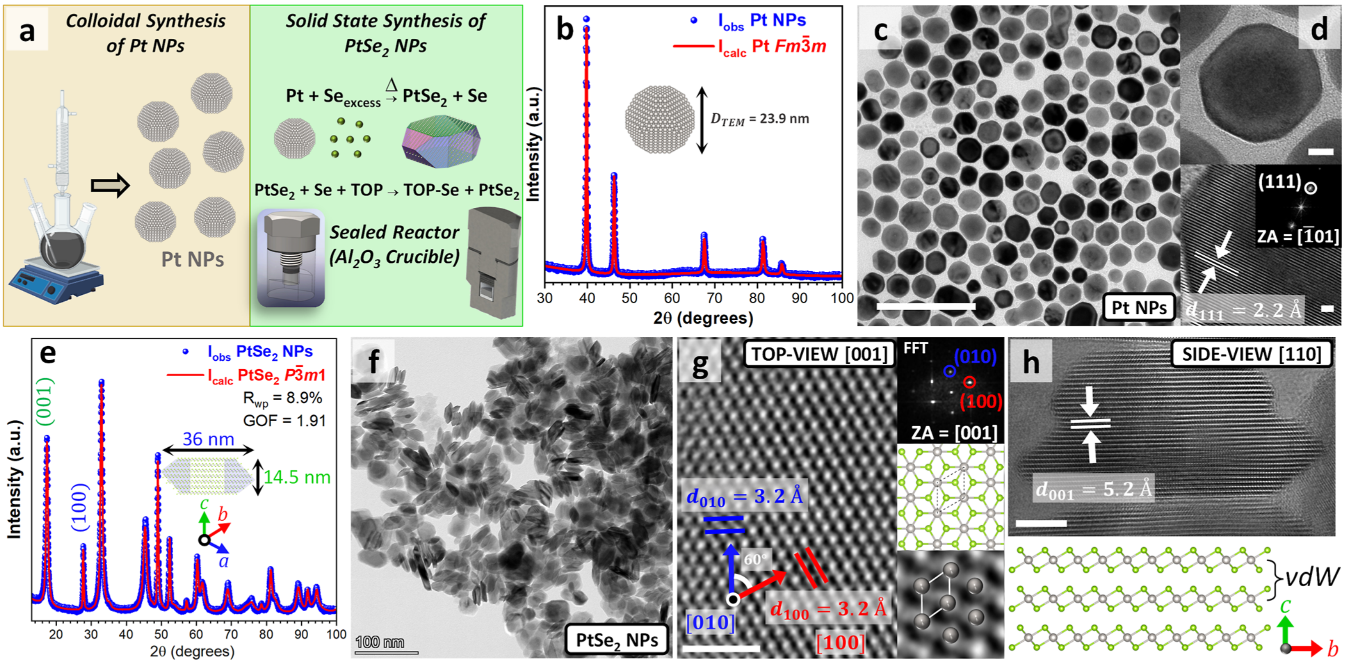

Figure 1. Synthesis and characterization of $PtSe_2$ NPs. (a) Schematics representing colloidal synthesis of Pt NPs followed by solid-state synthesis of $PtSe_2$ NPs in the homemade reactor; (b) XRD for Pt NPs showing the Rietveld refinement of the cubic cell ($Fm\bar{3}m$); (c) TEM of Pt NPs; (d) HRTEM of Pt NPs showing the well crystalline nanocrystals with lattice fringe of the (111) planes; (e) XRD for $PtSe_2$ NPs and Le Bail refinement for the trigonal space group ($P\bar{3}m1$); inset shows a model of the indexed NP shape with its average crystallite size calculated for the [001] and [100] directions; (f) TEM of $PtSe_2$ NPs; (g) HRTEM image showing the top-view aligned in the [001] zone axis of a single $PtSe_2$ NP and the indexed crystallographic planes (100) and (010) with spacing of 3.2 Å. (h) HRTEM image showing the side-view ([110] zone axis) of a $PtSe_2$ NP and its lattice fringe for (001) plane with spacing of 5.2 Å. The scale bar is (c) 100, (d) 5 (inset 2 nm), (f) 100, (g) 2, and (h) 5 nm.

(NPs).[16] Considering the advantage of having more exposed edges and surface defects, $PtSe_2$ NPs emerge as an interesting class of TMDs for HER applications.

Bulk $PtSe_2$ materials, including single crystals or polycrystalline material TMDs, are synthesized using sealed quartz tubes under vacuum either by chemical vapor transport methods or flux.[17,18] Most of those procedures have been used for decades to grow TMD materials, but the synthesis of controlled TMD NPs has not been extensively explored apart from 2D materials. Generally, the synthesis of $PtSe_2$ thin films or monolayers involves molecular beam epitaxy, chemical vapor deposition (CVD), or atomic layer deposition techniques, the latter being a specific method within CVD.[19,20] Those methods lead to high quality, thickness, and chemical control over $PtSe_2$ materials; however, they require a highly controlled environment and equipment.[8,21] For HER, the 2D TMDs synthetized by those methods require defect induction to improve the catalytic performance.[22] Alternatively, bulk $PtSe_2$ can be exfoliated to produce 2D thin films or monolayers instead of directly growing 2D TMDs by CVD methods. The weak vdW interactions along the *c*-axis, [001] crystallographic direction of 1T/2H structures,[23] can be broken through mechanical (scotch tape process), electrochemical, or chemical exfoliation methods to obtain 2D nanomaterials.[24,25] Notably, one of the most explored chemical processes is based on the lithium intercalation employing *n*-butyllithium (Bu-Li),[26] in which the small alkali metal donates electrons to the host material and penetrates its interlayers. The exfoliation occurs by a reaction of the intercalated product with water in an ultrasonic bath,[27,28] generating hydrogen and separating the 2D layers.[29,30] At the same time, Bu−Li also creates defects in the TMD product, as it has been reported that the concentration of defects depends upon the amount of Bu−Li used.[22,31] Short-time intercalations can also form dislocations at the edges of the solids;[32] transmission electron microscopy (TEM) experiments indicated that alkali ion insertion causes strain and defects are created to relax its lattice.[33,34]

$PtSe_2$'s electrochemical performance can be enhanced by the presence of defects and lowering its size.[15,35,36] $PtSe_2$ NPs have a higher surface/volume ratio compared to bulk, and, compared with 2D TMDs, NPs have a greater portion of the surface area composed by edges, leading to higher edge exposure. In the context of HER application, the H adsorption energy is much lower for the edges of a monolayer 1T-$PtSe_2$ (Gibbs free energies $\Delta GH^* = 0.07$ eV) compared to the basal plane ($\Delta GH^* = 1.07$ eV).[15] Consequently, it is expected that $PtSe_2$ NPs show improved electrochemical efficiency compared to those of even 2D TMDs. Additionally, instead of creating defects on the basal plane of 2D TMDs,[37] which are time-consuming and costly, defect engineering directly on $PtSe_2$ NPs can combine both HER performance requirement in a single catalyst. In this sense, it is known that Bu−Li treatment creates defects, and its reaction with $PtSe_2$ NPs is yet to be pursued. Therefore, controlling the reaction time is crucial for managing defects in the structure, especially in small particles subjected to similar conditions.

Our work explored the synthesis of $PtSe_2$ NPs by the selenization of the previously synthesized Pt NPs and its reaction with n-Bu−Li creating nanomaterials with no atomic long-range ordering (LRO, which has atomic periodicity longer than three unit cells)[38] and subsequently investigated the material as catalysts for HER. TEM, X-ray photoelectron spectroscopy (XPS), Raman spectroscopy, and pair distribution function from electron diffraction (ePDF) were used to

https://doi.org/10.1021/acs.chemmater.4c00753

fully characterize the atomic structure of $PtSe_2$ NPs and, by intentionally creating defects on $PtSe_2$, to correlate their atomic structure with their catalytic performance toward the HER.

■ RESULTS AND DISCUSSION

$PtSe_2$ NPs were synthesized by following a two-step procedure shown in Figure 1a. In the first step, Pt NPs were synthesized from the thermal decomposition of $Pt(acac)_2$ in oleylamine, which acts as the solvent, reducing agent, and surface ligand, whereas oleic acid was used as the second ligand. X-ray diffraction (XRD) results and the Rietveld refinement prove the formation of the cubic phase of metallic Pt, as shown in Figure 1b. TEM images were analyzed to determine the size, structure, and morphology of the NPs. The Pt NPs exhibited a predominant spherical shape, as shown in Figure 1c, and an average diameter of 23.9 nm, as shown in Figure S1. Additionally, HRTEM images revealed the lattice fringes of Pt with a *d*-spacing of 2.20 Å indexed to the (111) planes, as shown in Figure 1d. HRTEM also showed that Pt NPs are monocrystalline particles with low concentrations of defects such as twins and stacking faults.

The second step was the selenization of the Pt NPs by a solid-state reaction. The Pt NPs were mixed with excess of elemental Se and heated at 400 °C for 2 h using a homemade reactor, as shown in Figure 1a. The closed reactor designed was efficient, allowing for the complete selenization of Pt NPs. Rietveld refinement of the final $PtSe_2$ nanomaterial revealed the trigonal sudovikovite structure ($P\bar{3}m1$, PDF 18-0970) with R_{wp} of 8.9%, as shown in Figure 1e. XRD analysis also confirms that all Pt NPs were consumed in the reaction, forming $PtSe_2$, without metallic Pt remains or other secondary phases. As seen in Figure 1f, $PtSe_2$ NPs present an anisotropic shape that resembles nanoplates, which translates into an anisotropic peak broadening in the XRD pattern combining sharp and broadened peaks. The crystallite size calculated using Scherrer equation from the ⟨001⟩ direction (vdW distances, height) and the ⟨100⟩ direction, resulting in 14.5 nm of height and 36.0 nm of lateral size, respectively. This result is consistent with the morphology shown in TEM images with dimensions of around 30 nm (length, *ab*-plane) and 13 nm (height, *c*-axis), as shown in Figure 1f.

HRTEM analyses were performed to further enhance our understanding of the $PtSe_2$ structure. HRTEM images of the top view (Figure 1g) and side view (Figure 1h) of individual $PtSe_2$ particle NPs are presented. The fast Fourier transform (FFT) images and the crystallographic structure representation on the [001] (top view) and [110] (side view) directions are shown along with the HRTEM images to illustrate the observations. On the top-view image, the (001) facet displays the indexed directions [010] and [100] with calculated lattice distances $d_{(010)}$ (3.2 Å) and $d_{(100)}$ (3.2 Å), which matches with the known sudovikovite structure. Also, the angle between [010] and [100] vectors (≈60°) also agrees with the structure, corroborating the indexed [001] zone axis. In the side-view image shown in Figure 1h, the $d_{(001)}$ lattice fringe measured (5.20 Å) is slightly larger than the interplanar distance d_{hkl} of the (001) plane (5.08 Å), showing that the vdW layers of $PtSe_2$ NPs present a small relaxation related to size effects. Apart from the observed lattice distances calculated, the $PtSe_2$ NPs are highly crystalline, with a low concentration of crystallographic defects.

Comparing the initial Pt NPs and final $PtSe_2$ NP morphologies, it was observed that the product did not maintain the spheroidal form. Wang et al. showed that $PtSe_2$ NPs obtained via the thermal selenization process of the previously synthesized Pt nanocubes preserved the original shape.[39] Also, looking at NPs dimensions (7.5 nm for Pt and 11.5 nm for $PtSe_2$) from Wang's results,[39] the calculated ratio from the predicted volume of $PtSe_2$ from Pt selenization (calculated from the Pt number of mols and the expected $PtSe_2$ volume, V_{calc} = 1940 nm^3) and the observed $PtSe_2$ average volume (V_{obs} = 1520.9 nm^3) is close to the ideal value around 1. Wang's result indicates that one individual Pt nanoparticle creates a single $PtSe_2$ nanocube after the thermal selenization process. Here, the average spherical Pt NPs (23.9 nm), averaged from the distribution shown in Figure S1, led to $PtSe_2$ NPs with different morphologies compared to the previously Pt seeds, showing a nanoplate shape with a 36.0 nm (*ab*-plane) diameter and 14.5 nm height (*c*-axis direction). Analyzing the reaction pathway, the ratio from presumed calculated from reaction stoichiometry (V_{calc} = 32.874 nm^3) and observed (V_{obs} = 14.759 nm^3) volume of $PtSe_2$ was around 2.2, which indicates that each individual Pt seed generates other ∼2 $PtSe_2$ particles, as shown in Figure S2. Here, not only the shape of $PtSe_2$ was different from the seed but also the reaction of spherical Pt seeds in liquid selenium leads to a $PtSe_2$ nanoplate with mass, or number of moles, lower than the predicted value, indicating that fragmentation of the $PtSe_2$ particle occurs during the selenization process.

Analyzing several HRTEM images, it was observed that $PtSe_2$ NPs display some specific facets, as shown in Figure S3. Looking at HRTEM images at the [100] or [110] zone axis, here called the side view of $PtSe_2$ nanoplates, no facets related to (100) or (110) were found, as those facets should have a 90° angle to the basal plane (001). Instead, two facets with angles around 45 and 37° were present and indexed to ($2\bar{2}3$) and ($1\bar{1}2$), respectively. The calculated angles for facet ($2\bar{2}3$), 44.5°, and ($1\bar{1}2$), 37.5°, are close to the observed values, and Figure S4 illustrates the atomic arrangement on those facets. Analyzing these results, a sketch of $PtSe_2$ morphology is illustrated in Figure 1e and compared to a nanoplate having facets (100) or (110), as shown in Figure S3, to emphasize that the final $PtSe_2$ shape resembles the one presented in Figure 1e. As the height of $PtSe_2$ is smaller than the *ab*-plane, a possible fragmentation reaction pathway could occur by the cleavage of the vdW layers, generating more than one $PtSe_2$ particle by one Pt seed. The final proposed model is presented in Figure S2, indicating that one individual Pt (25.5 nm) can generate more than one nanoplate, exposing the facets ($2\bar{2}3$) and ($1\bar{1}2$) with a mean diameter of 35.7 and 14.5 nm of height. Based on the Wulf construction (Wulff's theorem), a nanomaterial with a given volume will present a specific shape attempting to minimize the total surface free energy. Several considerations should be made based on the process of synthesis, temperature, surface composition (ligands attached to the surface), and environment. However, here, the selenization process of Pt NPs in a liquid selenium reaction (excess of Se) led to $PtSe_2$ nanoplate preferably exposing the vdW facets (001) and the ($2\bar{2}3$) and ($1\bar{1}2$) facets, different from the thermal selenization observed by Wang et al.[39]

To create the defects in $PtSe_2$ NPs' structure, we conducted a liquid-phase reaction with Bu−Li assisted by water sonication, tuning the reaction, and the ultrasonic bathing

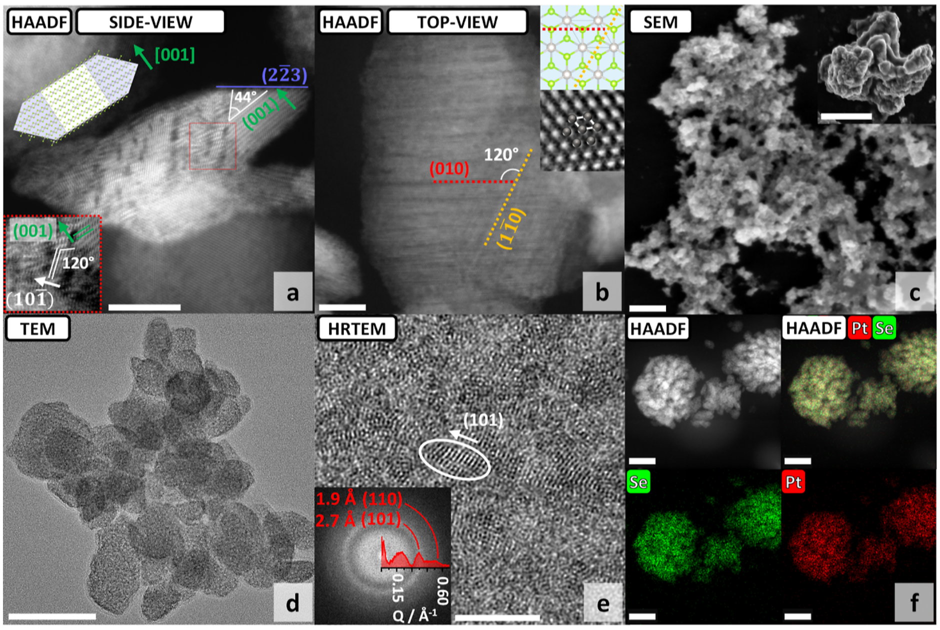

Figure 2. TEM and SEM images of Bu−Li-treated $PtSe_2$ NPs ($PtSe_x$ sample) showing two HAADF-STEM images of an intermediate reaction product in (a) side view and (b) top view [001] direction; (c) SEM image of the agglomerated material in the final product; (d) BF-TEM image of the fully broken structure; (e) HRTEM showing the presence of the SRO structure for the $PtSe_x$ sample; (f) EDS-STEM mapping of a fully broken structure. The scale bar is (a) 10, (b) 10, (c) 500 (inset 500 nm), (d) 50, (e) 5, and (f) 50 nm.

time. The product of this process was the cleavage of the covalent $PtSe_2$ bonds (here named $PtSe_x$), as seen by an intermediate state throughout the reaction of Bu−Li characterized by HRSTEM-HAADF and displayed in Figure 2a,b. Looking at a side view of an individual $PtSe_x$ nanocrystal around the [110] zone axis, which is orthogonal to the $(001)_{vdW}$ planes, the covalent bond within the vdW layers is being broken with an angle of 44° from the $(001)_{vdW}$ plane, indicating that the cleavage facet is the $(2\bar{2}3)$, as shown in Figure 2a. The inset also shows the $(001)_{vdW}$ planes with the green arrow in the [001] direction and the broken bounds region with increased contrast of the (101) planes. After breaking the LRO of nanocrystals, the visible contrast for $(001)_{vdW}$ planes becomes weaker and the (101) planes (I_{100} peak of diffraction) are easily seen in the TEM images. Looking at the top view of a single NP, as shown in Figure 2b, the broken bounds are seen as an alternate shadows contrast (darker and brighter contrast) parallel to (010) and $(1\bar{1}0)$ planes (around 120° of interplanar angle), shown using the red and orange lines, respectively. These shadow lines seen at the [001] direction are also parallel to the $(2\bar{2}3)$ plane, corroborating the indexation previously discussed at the side view. Instead of exfoliating the $PtSe_2$ NPs on the [001] direction, which was supposedly the weaker bound in the layered vdW structure,[40] the Bu−Li reaction led to the rupture Pt−Se bonds in *ab*-plane layers. Similar results have been previously reported in the literature, showing that chemical exfoliation with Bu−Li can affect the intralayer bonding between metals and chalcogenides and distort the octahedral structure of TMDs, such as MoS_2.[41] Other works have shown that the method can be ineffective for exfoliating selenides and tellurides without causing structural defects, as is the case of this study.[42] Previously, TEM results also reported the creation of "cracks" on the MoS_2 structure, which are a result of lattice relaxation after the creation of strain by lithium insertion.[33,34]

The SEM image of the $PtSe_x$ sample shows agglomerated regions resembling amorphous disordered materials, and the inset is presented to highlight the morphology of $PtSe_x$ in the absence of the previous $PtSe_2$ NPs shape, as shown in Figure 2c. TEM/scanning TEM (STEM) was used to understand the atomic short-range ordering (SRO) (first atomic neighbors)[43] of the $PtSe_x$ sample, as shown in Figure 2d−f. TEM images of $PtSe_x$ resemble the shape of its precursor $PtSe_2$ NPs with no visible LRO (lattice fringes). Instead, high-frequency contrast, dark and clear regions within the particle are seen, indicating low crystalline regions like clusters. Figure 2e presents the HRTEM image that shows a crystalline $PtSe_x$ structure keeping only the atomic SRO. An FFT image of this area revealed the frequencies of the (101) and (110) planes of the $P\bar{3}m1$ $PtSe_2$ phase with d_{hkl} values of 2.7 and 1.9 Å, respectively. On the HRTEM image, it is possible to visualize small areas where the (101) aligned planes are seen on regions of few nanometers. As the (101) plane is the facet with a higher structure factor intensity F_{hkl} (I_{100} on XRD), the HRTEM result revealed only those lattice fringes and the (001) vdW frequencies were not directly visualized by HRTEM. These analyses indicate that the $PtSe_x$ sample is still a crystalline sample with small crystallite sizes. STEM high-angle annular dark field (HAADF) characterization was performed along with chemical analysis (energy-dispersive X-ray spectroscopy, EDS) to understand the Pt and Se atomic distribution for $PtSe_x$ samples. Figure 2f shows a uniform distribution of Pt and Se elements around the NPs with an atomic ratio (Se/Pt = 1.8), which is smaller than that of $PtSe_2$ (Se/Pt = 2.4). Although EDS analysis is a semiquantitative technique, three areas were analyzed showing the same trend. Moreover, XPS analysis corroborates the decrease of the Se amount for $PtSe_x$ (1.9) compared to that for $PtSe_2$ (2.2). Both techniques indicate the formation of selenium vacancies in $PtSe_x$ samples. The Se/Pt ratio also points to a preservation of the low-range ordering, as completely amorphous $PtSe_x$ phases were synthesized in other studies with a lower Se/Pt ratio.[44]

The chemical composition of the samples was probed by XPS analysis before and after treatment with Bu−Li. Pt 4f and Se 3d spectra are shown in Figure 3. Before treatment, $PtSe_2$ presents one main contribution from Pt $4f_{7/2}$ at 73.2 eV (green peak) due to Pt^{4+}on the $PtSe_2$ structure and a minor contribution of about 5% at 72.1 eV (pink peak) due to defects on the surface of the particles or different Pt chemical environments.[45] On the Se 3d spectrum, only one species of Se could be identified at 55.6 eV for Se $3d_{5/2}$, although both doublet peaks ($3d_{5/2}$ and $3d_{3/2}$) are close due to the small spin orbit splitting. The higher intensity for the $Pt4f_{7/2}$ peak at 72.0 eV (orange peak) was attributed for higher contribution of defects for the $PtSe_x$ sample induced by the Bu−Li treatment. Although the Se 3d spectrum could be fitted with one species at 54.8 eV (Se $3d_{5/2}$), the bands are much larger (fwhm = 1.8 eV) than for the pristine NPs (fwhm = 0.9 eV), which indicates that more than one chemical environment for Se could be present. The XPS result also corroborates the EDS chemical mapping analysis from STEM, indicating a higher concentration of defects after Bu−Li treatment. Finally, no indication of metallic Pt was observed, which would be present at 71 eV.

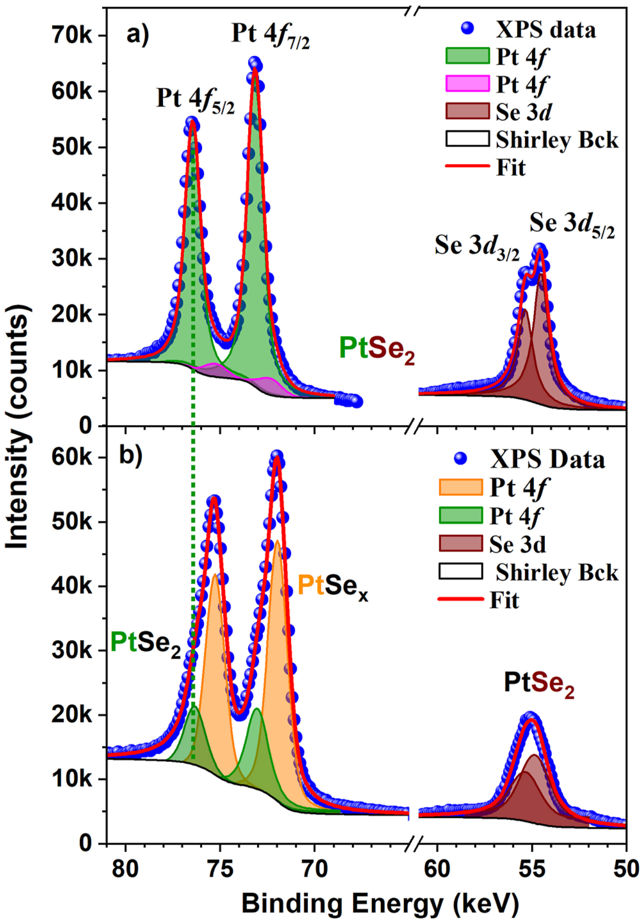

Figure 3. High-resolution XPS spectra of $PtSe_2$ and $PtSe_x$ NPs for Pt 4f and Se 3d regions.

In XRD analysis of $PtSe_x$, the Le Bail fitting revealed the presence of a small amount of a crystalline phase (green peaks, 13%), but most of the signal is diffuse scattering attributed to a disordered phase (broadened orange peaks, 87%), as shown in Figure 4a. The absence of LRO ordering for $PtSe_x$ contributes to the XRD peak broadening, even though HRTEM has shown that the sample preserves the SRO. Figure 4b depicts the Raman spectra of the $PtSe_2$ and $PtSe_x$ samples. Before Bu−Li treatment, it was possible to observe two active Raman modes, the E_g and A_1 peaks at 178 and 206 cm^{-1}, which correspond to in-plane and out-of-plane vibrations, respectively. These modes are classified as first-order phonon emissions.[46] The longitudinal optical (LO) vibrational mode can also be observed at 228 cm^{-1} as a small peak shoulder of the right side of the A_{1g} peak. This mode is composed of the A_{2u}, corresponding to out-plane, and E_u, the in-plane antisymmetric vibrations. After Bu−Li treatment, A_{1g} and E_g peaks are shifted to lower energies by 1.57 cm^{-1}. Raman spectroscopy agrees with the other structural analyses indicating that $PtSe_x$ keeps the SRO and their local Pt−Se atomic arrangement as proved by the presence of A_{1g} and E_g peaks. Additionally, a fourth peak at 60 cm^{-1} appears, which was attributed to the acoustic longitudinal (LA) mode.[47] The LA peak has been reported in the literature as originating from defects, which is expected, as the $PtSe_x$ sample synthesized here was revealed to be a disordered material by HRTEM.

The ePDF technique is an outstanding characterization tool for disordered materials,[48−50] which can be calculated by the Fourier transform of the structure factor $S(Q)$ obtained from the electron diffraction pattern; see Figure S5. Figure 4c shows the ePDF $G(r)$ analysis for $PtSe_x$ indicating the absence of atomic ordering after 1 nm. The first $G(r)$ peak corresponds to the Pt−Se interatomic distance at 2.47 Å, and at least four other broadened (overlapped) peaks are seen in the ePDF data. The contribution from the first Se−Se (light blue) at 3.33 Å indicated by the $G(r)$ partials are almost absent in the $PtSe_x$, as the second $G(r)$ peak has lower intensities around 3.3 Å that the simulated signal (blue) for ordered $PtSe_2$ structure, suggesting higher atomic disorder for $PtSe_x$. The second $G(r)$ peak is composed mostly of the Pt−Pt signals at 3.73 Å, as expected by the higher scattering factor for Pt atoms. Also, no other $G(r)$ peaks from metallic platinum or oxidation were found in the ePDF result. All the structural characterization performed here, such as HRTEM, Raman, and ePDF, confirm that creating defects by reacting PtSe2 NPs with Bu−Li leads to breaking the in-plane covalent bonds, resulting in $PtSe_x$ nanostructures keeping the SRO of the $PtSe_2$ $P\bar{3}m1$ phase.

The electrocatalytic performance of $PtSe_2$ and $PtSe_x$ was investigated toward the HER and compared to Pt NPs. The literature presents Pt/C (Pt supported in carbon) as an ideal electrocatalyst for HER; here, Pt curves are presented as a reference material with comparable size and electrode preparation method. The HER polarization curves of Pt (black), $PtSe_2$ (green), and $PtSe_x$ (orange) NPs are displayed in Figure 5a, showing the increased catalytic performance of $PtSe_x$ compared to $PtSe_2$ NPs. Three indicators were considered to assess the electrochemical performance, the onset potential, overpotential at −10 mA cm^{-2} (j_{10}), and the Tafel slope. First, the onset potential was estimated at −0.1 mA cm^{-2} and the $PtSe_x$ showed a smaller onset at 74 mV than $PtSe_2$ (105 mV) and, as expected, both are higher than Pt (13 mV). The j_{10} values for $PtSe_x$ (269 mV) and $PtSe_2$ (340 mV) NPs demonstrate that $PtSe_x$ has better electrocatalytic performance. The electrochemical surface area (ECSA) was determined for $PtSe_2$ and $PtSe_x$ through measurements of the double-layer capacitance, showing a 16% increase in the active area after defect creation, as shown in Figure S7. The

https://doi.org/10.1021/acs.chemmater.4c00753
Chem. Mater. 2024, 36, 8613−8622

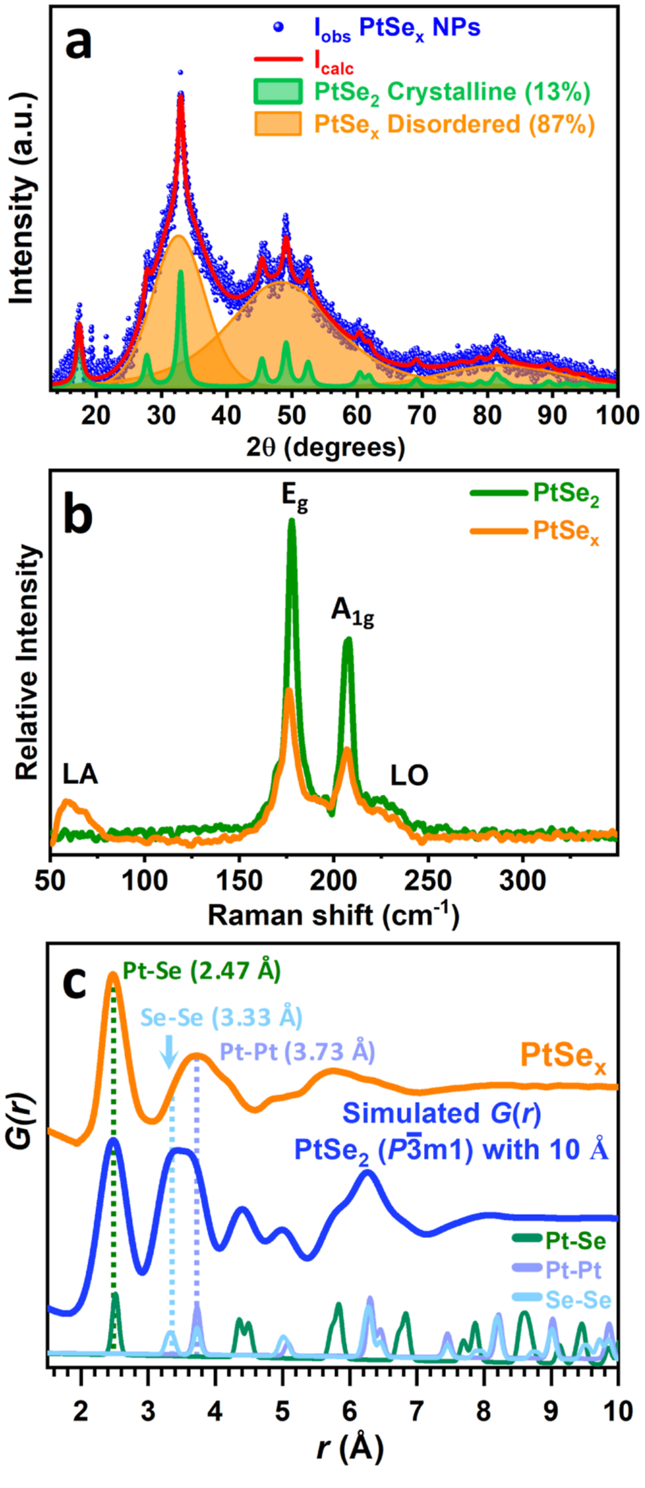

Figure 4. Structure analysis of the $PtSe_x$. (a) XRD pattern with Le Bail fitting for the $PtSe_2$ trigonal space group (green peaks) and the diffuse scattering (orange) attributed to defected $PtSe_x$; (b) Raman spectrum of the $PtSe_2$ and $PtSe_x$ samples showing the typical E_g, A_{1g}, and LO peaks for both structures and the appearance of the LA peak at low Raman shift for the $PtSe_x$ sample. $PtSe_x$ also display a small shift for E_g and A_{1g} peaks; (c) ePDF $G(r)$ for $PtSe_x$ NPs and simulated $PtSe_2$ crystal of 10 Å. The simulated $G(r)$ partials are displayed showing the Pt−Se (green), Pt−Pt (purple), and Se−Se (light blue) contributions for the total ePDF $G(r)$ result. The first main three coordination shell peaks are also labeled, indicating that the SRO of $PtSe_x$ remains preserved compared to $PtSe_2$ ($P\bar{3}m1$).

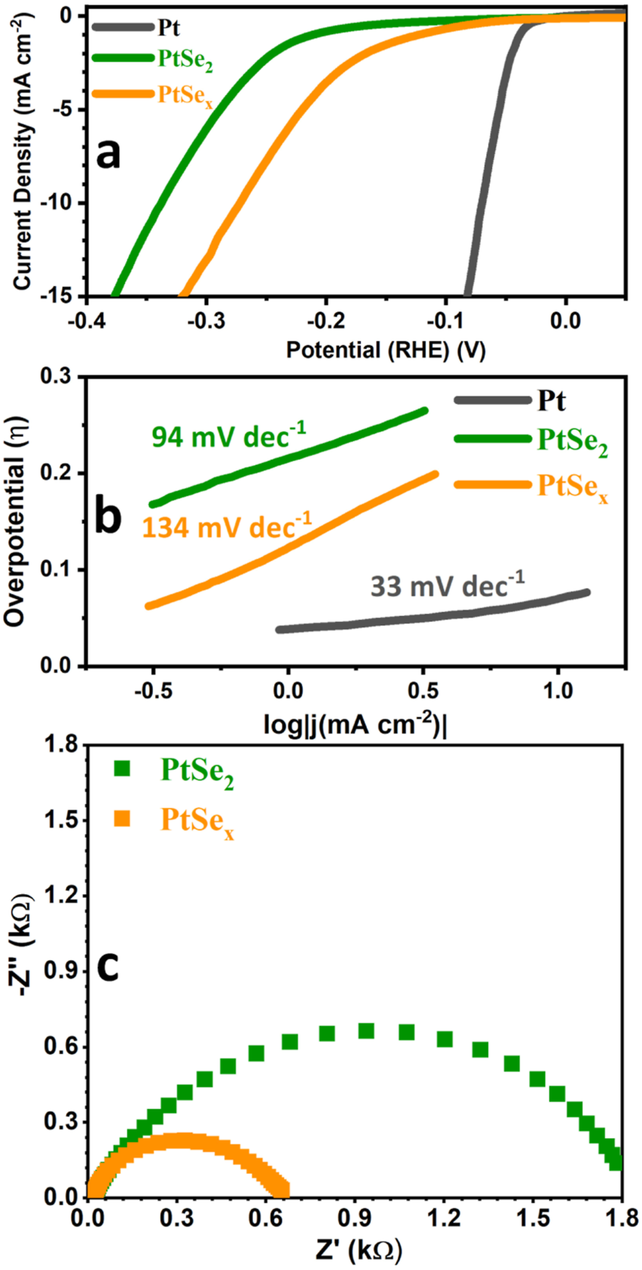

Figure 5. HER properties of $PtSe_2$ and $PtSe_x$ NPs. (a) Linear sweep voltammograms versus the RHE for HER on Pt, $PtSe_2$ and $PtSe_x$ NPs; (b) Tafel plots for Pt, $PtSe_2$ and $PtSe_x$ NPs; (c) EIS for the $PtSe_2$ and $PtSe_x$.

measurements were conducted using literature methods.[51,52] Moreover, both $PtSe_2$ and $PtSe_x$ have better efficiency than bulk $PtSe_2$ and 2D monolayers from the literature.[53,54] A chronoamperometry at 0.3 V was conducted to assess the $PtSe_x$ electrochemical stability, as shown in Figure S8, and the chemical stability was tested by letting the NPs rest in water for 2 weeks, as shown in Figure S9. The chronoamperometry shows a 14% efficiency decay after 20 min of reaction, most likely due to the formation of hydrogen bubbles that prevent mass diffusion in the catalyst/electrolyte interface. Compared to the literature, $PtSe_2$ is a sturdy catalyst toward HER and long-term stability is expected using specific electrolyzer devices as thin films.[44,55] The Tafel slope is defined as the increase in overpotential required to produce a significant rise in current density.[53] For HER, the literature shows that Pt/C NPs typically exhibit a Tafel slope of 30 to 40 mV/dec^{-1}, and the synthesized Pt NPs achieved a Tafel slope of 33 mV/dec^{-1}, as shown in Figure 5b. A notable difference was observed in the Tafel slope of $PtSe_x$ and $PtSe_2$ NPs estimated as 143 and 95 mV/dec^{-1}, respectively. Electrochemical impedance spectroscopy (EIS) was performed to assess the processes occurring in the system. As can be seen in Figure 5c, a single semicircle is observed in the Nyquist complex-impedance plot for both $PtSe_x$ and $PtSe_2$ NPs. Interestingly, the diameter of the semicircle obtained for $PtSe_x$ is smaller than that measured for $PtSe_2$ NPs, demonstrating better conductivity, which contributes to the performance for the evolution reaction. To gain a deeper understanding of the charge transfer phenomena, the experimental impedance spectra were fitted by using an equivalent circuit model (Table S1). In the employed circuit, R_{ct} represents the charge transfer resistance, which is lower for the $PtSe_x$ confirming its better carrier mobility. Despite having a higher Tafel slope, $PtSe_x$ demonstrated better performance at −10 mA cm^{-2} due to its superior conductivity, as observed in EIS. The improved electrocatalytic performance shown by the chemically modified sample is likely a result of a combination of factors. XPS has also shown that the Pt chemical environment contribution for Pt $4f_{7/2}$ at ~72 eV is much higher than the atomic sites Pt $4f_{7/2}$ at 73.2 eV for the $PtSe_x$ sample, demonstrating that the chemical state of Pt for $PtSe_x$ is different, which could also impact the electrocatalytic performance. The TEM analyses proved that $PtSe_x$ exposes higher surface area with unusual crystallographic facets, which could serve as additional active sites for hydrogen adsorption, compared to standard catalytic performance from the literature that probe the basal plane (001) and its defects.[9,18] The disruption of the LRO for $PtSe_x$ compared to $PtSe_2$ NPs seems to also support the enhancement of charge carrier mobility, and further investigation is necessary to understand all the influences of breaking the structure on the electronic transport, not only on electrochemical reactions. The literature is scarce on HER for $PtSe_2$ NPs, and our results can shed light on the possibility of using $PtSe_x$ NPs as catalysts for the cathodic reaction. To comprehend the full potential of $PtSe_2$ NPs for HER, additional studies should be conducted.

CONCLUSIONS

Overall, a novel method to synthesize high quality $PtSe_2$ NPs in a fast and simple procedure is presented. Using previously synthesized Pt NPs, the size and shape of $PtSe_2$ were controlled, leading to crystalline nanopellets. The $PtSe_2$ reaction with Bu−Li led to cleavage of the covalent bound along the *ab*-plane of 2D monolayers (intralayer) and broke the $PtSe_2$ long-range structure. The result was a $PtSe_x$ nanomaterial with a small deselenization process having only the SRO but keeping the local structure, as proved by Raman and ePDF analyses. The XPS also revealed that an increase in a low-coordination Pt environment occurred. Both NPs' performance toward the HER application were tested indicating a better efficiency compared to bulk $PtSe_2$ and 2D monolayers from the literature. Therefore, the results reported here indicate that $PtSe_2$ NPs can be produced in a fast and simple method compared to the standard selenization process being useful as an electrocatalyst toward HER. The findings also demonstrate the potential replacement of Pt metallic cathodes with $PtSe_2$. Future advances in $PtSe_2$ NPs including dopants, defects control, and nano heterojunctions studies could improve its performance.

EXPERIMENTAL SECTION

Synthesis of Platinum Nanoparticles. Pt NPs were synthesized with 0.20 mmol of platinum acetylacetonate(II) (97%) and 1.0 mmol of oleic acid (90%) in 10.0 mL of oleylamine (70%), which were obtained from Aldrich Chemical. The reaction occurred in a closed reaction system composed of a three-neck flask (50.0 mL), which was first heated at 80 °C for 30 min under vacuum for degassing. Afterward, the temperature was raised to 250 °C for 1 h in a nitrogen atmosphere and then cooled to room temperature. The colloidal solution was washed with the addition of isopropanol (heated at 40 °C), followed by centrifugation at 9000 rpm. The precipitate was redispersed in toluene, and this purification procedure was repeated at least 3 times. Finally, the Pt NPs product was redispersed in toluene and stocked.

Synthesis of Platinum Selenide Nanoparticles and *n*-Butyllithium Treatment. The Pt NPs were dried in vacuum and mixed with excess selenium, approximately in a molar ratio of 4:1. The mixture was sealed in a homemade stainless-steel reactor with an interior of high purity alumina (Al_2O_3) ceramic TGA pan under an inert N_2 atmosphere inside a glovebox; see Figure 1a for the illustration of the reactor. The reactor was then heated to 400 °C for 2 h in a muffle furnace. After cooling, excess selenium was solubilized with trioctylphosphine (TOP) and separated via centrifugation under an inert condition. The material was purified by adding acetone, followed by centrifugation at 9000 rpm and discarding of the supernatant. This purification was repeated 3 times, and the material was dried under vacuum for storage.

To create defects in the $PtSe_2$, a controlled reaction was conducted with *n*-butyllithium (Bu−Li, 1.6 M in hexane, Sigma-Aldrich) by adding 1 mL of Bu−Li solution and 1 mL of hexane to 78.0 mg of $PtSe_2$ in a glass vial. Then, the mixture was stirred at room temperature for 10 min, followed by 15 min in an ultrasonic bath. After this procedure, the mixture was sequentially washed with hexane, acetone, and deionized water to eliminate the LiOH byproduct.

Material Characterization. TEM and high-resolution TEM (HRTEM) images were obtained on a JEOL JEM-2100F operating at 200 kV. STEM, electron X-ray dispersive spectroscopy (EDS) mapping, and HAADF analyses were carried out on the Thermo Fisher/FEI Titan Cubed Themis double corrected microscope operating at 300 kV. The ePDF analysis was calculated using the method previously optimized by our group, and the detailed procedure can be found elsewhere.[48−50] Briefly, by collecting 16 electron diffraction images, the Gatan DigitalMicrograph Software (GMS 3) was used to align and sum, and after the azimuthal integration, the $I(Q)$ experimental data were obtained.[47] The eRDF software[56] was used to calculate the structural factor $S(Q)$; see Figure S5 in the Supporting Information and the final ePDF $G(r)$ result. PDF $G(r)$ simulation was calculated using the T. Proffen and R.B. Neder software DISCUS.[57,58] XRD data were collected in a Bruker D8 Advance ECO using a Cu Kα (λ = 0.15406 nm) source, a linear detector LYNXEYE XE (PSD of 2.948°), a primary optics (2.5° axial soller and 0.6 mm slit), and a secondary optics (2.5° axial soller and 5.4 mm slit). Raman spectroscopy data were collected using a XploRA PLUS Confocal Raman Spectrometer using a 638 nm laser and grating of 2400 gr/mm. XPS experiments were performed with K-alpha surface analysis (Thermo Scientific) equipment with an Al Kα X-ray source (1486.6 eV) and a flood gun. The investigated area was an ellipse of approximately 300 μm in diameter, and three different areas of each sample were examined. Ten scans for high-resolution spectra were carried out for Se 3d and Pt 4f, with a pass energy of 50 eV, energy step size of 0.10 eV, and a dwell time of 50 ms. Peaks were fitted by using the Avantage software (Thermo Scientific). The binding energy of the spectra was corrected with that of adventitious carbon C 1s (C−C and C−H) at 284.8 eV.

Electrochemical Characterization. The electrochemical measurements were conducted by using a standard three-necked electrochemical cell. For the working electrode, a dispersion of $PtSe_2$ NPs in a mixture of 2-propanol and deionized water was applied onto a glassy carbon electrode. The amount of dispersion deposited was precisely measured to achieve a coverage of 100 μg cm^{-2}. Platinum was used as a counter electrode, and the reference electrode was an Ag/AgCl in a saturated KCl solution. The Metrohm μAutolab III potentiostat was set to 10 mV s^{-1} scan rate, and sweep was performed from 0 to −0.6 V vs reversible hydrogen electrode (RHE). For the electrochemical impedance measurements, a constant potential of −0.32 V vs RHE was applied in a sweep range of 100 kHz to 1 Hz with an AC amplitude of 10 mV.

■ ASSOCIATED CONTENT

Supporting Information

The Supporting Information is available free of charge at https://pubs.acs.org/doi/10.1021/acs.chemmater.4c00753.

> Pt NPs histogram of counting; scheme of the proposed model for $PtSe_2$ NP formation from the selenization of Pt NPs; HRTEM images of $PtSe_2$ borders; $PtSe_2$ NPs 3D model with their facets indexed; electron diffraction images, the electron diffraction intensity profile $I(Q)$, normalized structural factor $S(Q)$ used to calculate the ePDF; additional voltammetries for the $PtSe_2$ and $PtSe_x$; electrochemical results summary; electrochemical surface area analysis; chronoamperometry for the $PtSe_x$ sample; TEM images and XPS spectra for the $PtSe_x$ after 2 weeks in water (PDF)

■ AUTHOR INFORMATION

Corresponding Author

João Batista Souza Junior − *Brazilian Nanotechnology National Laboratory (LNNano, Brazilian Center for Research in Energy and Materials (CNPEM)), 13083-100 Campinas, Brazil; Institute of Chemistry, University of Campinas (UNICAMP), 13083-970 Campinas, São Paulo, Brazil;* orcid.org/0000-0002-1725-3552; Email: joao.junior@lnnano.cnpem.br

Authors

Victor Secco Lemos − *Brazilian Nanotechnology National Laboratory (LNNano, Brazilian Center for Research in Energy and Materials (CNPEM)), 13083-100 Campinas, Brazil; Institute of Chemistry, University of Campinas (UNICAMP), 13083-970 Campinas, São Paulo, Brazil;* orcid.org/0000-0001-7960-6280

Daniel Angeli de Moraes − *Brazilian Nanotechnology National Laboratory (LNNano, Brazilian Center for Research in Energy and Materials (CNPEM)), 13083-100 Campinas, Brazil; Institute of Chemistry of São Carlos, University of São Paulo (USP), 13566-590 São Carlos, São Paulo, Brazil;* orcid.org/0000-0002-3711-1156

Iara de Lacerda Pataca − *Brazilian Nanotechnology National Laboratory (LNNano, Brazilian Center for Research in Energy and Materials (CNPEM)), 13083-100 Campinas, Brazil; Institute of Chemistry, University of Campinas (UNICAMP), 13083-970 Campinas, São Paulo, Brazil;* orcid.org/0000-0003-4965-9650

Olavo Fiamencini Verruma − *Brazilian Nanotechnology National Laboratory (LNNano, Brazilian Center for Research in Energy and Materials (CNPEM)), 13083-100 Campinas, Brazil; Institute of Chemistry, University of Campinas (UNICAMP), 13083-970 Campinas, São Paulo, Brazil;* orcid.org/0000-0003-4346-9063

Carolina Pirogini Torres − *Brazilian Nanotechnology National Laboratory (LNNano, Brazilian Center for Research in Energy and Materials (CNPEM)), 13083-100 Campinas, Brazil;* orcid.org/0009-0000-4468-0464

Angela Albuquerque − *Brazilian Nanotechnology National Laboratory (LNNano, Brazilian Center for Research in Energy and Materials (CNPEM)), 13083-100 Campinas, Brazil*

Ingrid Rodríguez-Gutiérrez − *Brazilian Nanotechnology National Laboratory (LNNano, Brazilian Center for Research in Energy and Materials (CNPEM)), 13083-100 Campinas, Brazil*

Danilo Biazon Janes − *Brazilian Nanotechnology National Laboratory (LNNano, Brazilian Center for Research in Energy and Materials (CNPEM)), 13083-100 Campinas, Brazil*

Felipe Crasto de Lima − *Ilum School of Science, CNPEM, 13083-100 Campinas, Brazil;* orcid.org/0000-0002-2937-2620

Flavio Leandro Souza − *Brazilian Nanotechnology National Laboratory (LNNano, Brazilian Center for Research in Energy and Materials (CNPEM)), 13083-100 Campinas, Brazil; Institute of Chemistry, University of Campinas (UNICAMP), 13083-970 Campinas, São Paulo, Brazil; Federal University of ABC (UFABC), 09210-580 Santo André, São Paulo, Brazil;* orcid.org/0000-0003-2036-9123

Edson Roberto Leite − *Brazilian Nanotechnology National Laboratory (LNNano, Brazilian Center for Research in Energy and Materials (CNPEM)), 13083-100 Campinas, Brazil; Department of Chemistry, Federal University of São Carlos (UFSCAR), 13565-905 São Carlos, São Paulo, Brazil;* orcid.org/0000-0002-0513-9939

Adalberto Fazzio − *Brazilian Nanotechnology National Laboratory (LNNano, Brazilian Center for Research in Energy and Materials (CNPEM)), 13083-100 Campinas, Brazil; Ilum School of Science, CNPEM, 13083-100 Campinas, Brazil*

Complete contact information is available at: https://pubs.acs.org/10.1021/acs.chemmater.4c00753

Author Contributions

The manuscript was written through contributions of all authors. All authors have given approval to the final version of the manuscript.

Notes

The authors declare no competing financial interest.

■ ACKNOWLEDGMENTS

This work was supported by Brazilian agency Fundação de Amparo à Pesquisa do Estado de São Paulo—FAPESP (Grants Nos. 2021/03321-9, 2022/13144-0, 2023/00984-2, and CEPID 2013/07296-2) and FINEP (MQSM).

■ REFERENCES

(1) Roduner, E. Size Matters: Why Nanomaterials Are Different. *Chem. Soc. Rev.* **2006**, *35*, 583−592.

(2) Manzeli, S.; Ovchinnikov, D.; Pasquier, D.; Yazyev, O. V.; Kis, A. 2D Transition Metal Dichalcogenides. *Nat. Rev. Mater.* **2017**, *2*, 17033−17115.

(3) Zhang, H.; Chhowalla, M.; Liu, Z. 2D Nanomaterials: Graphene and Transition Metal Dichalcogenides. *Chem. Soc. Rev.* **2018**, *47*, 3015−3017.

(4) Zhu, Y.; Peng, L.; Fang, Z.; Yan, C.; Zhang, X.; Yu, G. Structural Engineering of 2D Nanomaterials for Energy Storage and Catalysis. *Adv. Mater.* **2018**, *30*, 1706347.

(5) Han, G. H.; Duong, D. L.; Keum, D. H.; Yun, S. J.; Lee, Y. H. Van Der Waals Metallic Transition Metal Dichalcogenides. *Chem. Rev.* **2018**, *118*, 6297−6336.

(6) Tedstone, A. A.; Lewis, D. J.; O'Brien, P. Synthesis, Properties, and Applications of Transition Metal-Doped Layered Transition Metal Dichalcogenides. *Chem. Mater.* **2016**, *28*, 1965−1974.

(7) Wang, Y.; Li, L.; Yao, W.; Song, S.; Sun, J. T.; Pan, J.; Ren, X.; Li, C.; Okunishi, E.; Wang, Y. Q.; et al. Monolayer PtSe2, a New Semiconducting Transition-Metal-Dichalcogenide, Epitaxially Grown by Direct Selenization of Pt. *Nano Lett.* **2015**, *15*, 4013−4018.

(8) Gong, Y.; Lin, Z.; Chen, Y. X.; Khan, Q.; Wang, C.; Zhang, B.; Nie, G.; Xie, N.; Li, D. Two-Dimensional Platinum Diselenide: Synthesis, Emerging Applications, and Future Challenges. *Nano-Micro Lett.* **2020**, *12*, 174−234.

(9) Florindo, B. R.; Hasimoto, L. H.; de Freitas, N.; Candiotto, G.; Lima, E. N.; de Lourenço, C.; de Araujo, A. B. S.; Ospina, C.; Bettini, J.; Leite, E. R.; et al. Patterning Edge-like Defects and Tuning Defective Areas on the Basal Plane of Ultra-Large MoS2 Monolayers toward the Hydrogen Evolution Reaction. *J. Mater. Chem. A* **2023**, *11*, 19890−19899.

(10) Mak, K. F.; Lee, C.; Hone, J.; Shan, J.; Heinz, T. F. Atomically Thin MoS: A New Direct-Gap Semiconductor. *Phys. Rev. Lett.* **2010**, *105*, 136805.

(11) Voiry, D.; Yang, J.; Chhowalla, M. Recent Strategies for Improving the Catalytic Activity of 2D TMD Nanosheets Toward the Hydrogen Evolution Reaction. *Adv. Mater.* **2016**, *28*, 6197−6206.

(12) Crasto De Lima, F.; Fazzio, A. At the Verge of Topology: Vacancy-Driven Quantum Spin Hall in Trivial Insulators. *Nano Lett.* **2021**, *21*, 9398−9402.

(13) Crasto de Lima, F.; Focassio, B.; Miwa, R. H.; Fazzio, A. Topological Insulating Phase Arising in Transition Metal Dichalcogenide Alloy. *2d Mater* **2023**, *10*, 035001.

(14) Schoop, L. M.; Pielnhofer, F.; Lotsch, B. V. Chemical Principles of Topological Semimetals. *Chem. Mater.* **2018**, *30*, 3155−3176.

(15) Shi, J.; Huan, Y.; Hong, M.; Xu, R.; Yang, P.; Zhang, Z.; Zou, X.; Zhang, Y. Chemical Vapor Deposition Grown Large-Scale Atomically Thin Platinum Diselenide with Semimetal-Semiconductor Transition. *ACS Nano* **2019**, *13*, 8442−8451.

(16) Wang, Z.; Li, Q.; Besenbacher, F.; Dong, M. Facile Synthesis of Single Crystal PtSe$_2$ Nanosheets for Nanoscale Electronics. *Adv. Mater.* **2016**, *28*, 10224−10229.

(17) Hu, D.; Zhao, T.; Ping, X.; Zheng, H.; Xing, L.; Liu, X.; Zheng, J.; Sun, L.; Gu, L.; Tao, C.; et al. Unveiling the Layer-Dependent Catalytic Activity of PtSe2 Atomic Crystals for the Hydrogen Evolution Reaction. *Angew. Chem., Int. Ed.* **2019**, *58*, 6977−6981.

(18) Zhao, Y.; Qiao, J.; Yu, Z.; Yu, P.; Xu, K.; Lau, S. P.; Zhou, W.; Liu, Z.; Wang, X.; Ji, W.; Chai, Y. High-Electron-Mobility and Air-Stable 2D Layered PtSe2 FETs. *Adv. Mater.* **2017**, *29*, 1604230.

(19) Yan, M.; Wang, E.; Zhou, X.; Zhang, G.; Zhang, H.; Zhang, K.; Yao, W.; Lu, N.; Yang, S.; Wu, S.; et al. High Quality Atomically Thin PtSe2 Films Grown by Molecular Beam Epitaxy. *2d Mater.* **2017**, *4*, 045015.

(20) Xu, H.; Zhang, H.; Liu, Y.; Zhang, S.; Sun, Y.; Guo, Z.; Sheng, Y.; Wang, X.; Luo, C.; Wu, X.; et al. Controlled Doping of Wafer-Scale PtSe2 Films for Device Application. *Adv. Funct. Mater.* **2019**, *29*, 1805614.

(21) Li, J.; Kolekar, S.; Xin, Y.; Coelho, P. M.; Lasek, K.; Nugera, F. A.; Gutiérrez, H. R.; Batzill, M. Thermal Phase Control of Two-Dimensional Pt-Chalcogenide (Se and Te) Ultrathin Epitaxial Films and Nanocrystals. *Chem. Mater.* **2021**, *33*, 8018−8027.

(22) Zhou, L.; He, B.; Yang, Y.; He, Y. Facile approach to surface functionalized MoS2 nanosheets. *RSC Adv.* **2014**, *4*, 32570−32578.

(23) Zhang, Q.; Mei, L.; Cao, X.; Tang, Y.; Zeng, Z. Intercalation and Exfoliation Chemistries of Transition Metal Dichalcogenides. *J. Mater. Chem. A* **2020**, *8*, 15417−15444.

(24) Zhang, J.; Ji, T.; Jin, H.; Wang, Z.; Zhao, M.; He, D.; Luo, G.; Mao, B. Mild Liquid-Phase Exfoliation of Transition Metal Dichalcogenide Nanosheets for Hydrogen Evolution. *ACS Appl. Nano Mater.* **2022**, *5*, 8020−8028.

(25) Li, Y.; Kuang, G.; Jiao, Z.; Yao, L.; Duan, R. Recent Progress on the Mechanical Exfoliation of 2D Transition Metal Dichalcogenides. *Mater. Res. Express* **2022**, *9*, 122001.

(26) Shi, Y.; Zhang, H.; Chang, W. H.; Shin, H. S.; Li, L. J. Synthesis and Structure of Two-Dimensional Transition-Metal Dichalcogenides. *MRS Bull.* **2015**, *40*, 566−576.

(27) Voiry, D.; Yamaguchi, H.; Li, J.; Silva, R.; Alves, D. C. B.; Fujita, T.; Chen, M.; Asefa, T.; Shenoy, V. B.; Eda, G.; Chhowalla, M. Enhanced catalytic activity in strained chemically exfoliated WS2 nanosheets for hydrogen evolution. *Nat. Mater.* **2013**, *12*, 850−855.

(28) Benavente, E.; Santa Ana, M. A.; Mendizábal, F.; González, G. Intercalation Chemistry of Molybdenum Disulfide. *Coord. Chem. Rev.* **2002**, *224*, 87−109.

(29) Joensen, P.; Frindt, R. F.; Morrison, S. R. Single-Layer MoS$_2$. *Mater. Res. Bull.* **1986**, *21*, 457−461.

(30) Dines, M. B. Lithium intercalation via -Butyllithium of the layered transition metal dichalcogenides. *Mater. Res. Bull.* **1975**, *10*, 287−291.

(31) Knirsch, K. C.; Berner, N. C.; Nerl, H. C.; Cucinotta, C. S.; Gholamvand, Z.; McEvoy, N.; Wang, Z.; Abramovic, I.; Vecera, P.; Halik, M.; et al. Basal-Plane Functionalization of Chemically Exfoliated Molybdenum Disulfide by Diazonium Salts. *ACS Nano* **2015**, *9*, 6018−6030.

(32) Chrissafis, K.; Zamani, M.; Kambas, K.; Stoemenos, J.; Economou, N. A.; Samaras, I.; Julien, C. Structural Studies of MoS2 Intercalated by Lithium. *Mater. Sci. Eng., B* **1989**, 3, 145−151.

(33) Gao, P.; Wang, L.; Zhang, Y.; Huang, Y.; Liu, K. Atomic-Scale Probing of the Dynamics of Sodium Transport and Intercalation-Induced Phase Transformations in MoS$_2$. *ACS Nano* **2015**, *9*, 11296−11301.

(34) Ghosh, C.; Singh, M. K.; Parida, S.; Janish, M. T.; Dobley, A.; Dongare, A. M.; Carter, C. B. Phase evolution and structural modulation during in situ lithiation of MoS$_2$, WS$_2$ and graphite in TEM. *Sci. Rep.* **2021**, *11*, 9014.

(35) Tsai, C.; Chan, K.; Nørskov, J. K.; Abild-Pedersen, F. Theoretical Insights into the Hydrogen Evolution Activity of Layered Transition Metal Dichalcogenides. *Surf. Sci.* **2015**, *640*, 133−140.

(36) Huang, H.; Fan, X.; Singh, D. J.; Zheng, W. Modulation of Hydrogen Evolution Catalytic Activity of Basal Plane in Monolayer Platinum and Palladium Dichalcogenides. *ACS Omega* **2018**, 3, 10058−10065.

(37) Ma, L.; Shen, H. Activating PtSe$_2$ monolayer for hydrogen evolution reaction by defect engineering and Pd doping. *Appl. Surf. Sci.* **2021**, *545*, 149013.

(38) Kaduk, J. A.; Billinge, S. J. L.; Dinnebier, R. E.; Henderson, N.; Madsen, I.; Černý, R.; Leoni, M.; Lutterotti, L.; Thakral, S.; Chateigner, D. Powder diffraction. *Nat. Rev. Methods Primers* **2021**, *1*, 77.

(39) Wang, M.; Shawkat, M. S.; Xi, Z.; Xia, X.; Lee, K. S.; Son, D. I.; Bae, T. S.; Ryu, H. I.; Chung, H. S.; Jung, Y. Controllable Synthesis of Platinum Diselenide (PtSe$_2$) Inorganic Fullerene. *J. Mater. Chem. A* **2020**, *8*, 18925−18932.

(40) Janica, I.; Iglesias, D.; Ippolito, S.; Ciesielski, A.; Samorì, P. Effect of Temperature and Exfoliation Time on the Properties of Chemically Exfoliated MoS$_2$ Nanosheets. *Chem. Commun.* **2020**, *56*, 15573−15576.

(41) Jiménez Sandoval, S.; Yang, D.; Frindt, R. F.; Irwin, J. C. Raman Study and Lattice Dynamics of Single Molecular Layers of MoS$_2$. *Phys. Rev. B: Condens. Matter Mater. Phys.* **1991**, *44*, 3955−3962.

(42) O'neill, A.; Khan, U.; Coleman, J. N. Preparation of High Concentration Dispersions of Exfoliated MoS$_2$ with Increased Flake Size. *Chem. Mater.* **2012**, *24*, 2414−2421.

(43) Terban, M. W.; Billinge, S. J. L. Structural Analysis of Molecular Materials Using the Pair Distribution Function. *Chem. Rev.* **2022**, *122*, 1208−1272.

(44) He, Y.; Liu, L.; Zhu, C.; Guo, S.; Golani, P.; Koo, B.; Tang, P.; Zhao, Z.; Xu, M.; Zhu, C.; et al. Amorphizing noble metal chalcogenide catalysts at the single-layer limit towards hydrogen production. *Nat. Catal.* **2022**, *5*, 212−221.

(45) Sojková, M.; Dobročka, E.; Hutár, P.; Tašková, V.; Pribusová Slušná, L.; Stoklas, R.; Píš, I.; Bondino, F.; Munnik, F.; Hulman, M. High Carrier Mobility Epitaxially Aligned PtSe$_2$ Films Grown by One-Zone Selenization. *Appl. Surf. Sci.* **2021**, *538*, 147936.

(46) Ansari, L.; Monaghan, S.; McEvoy, N.; Coileáin, C. Ó.; Cullen, C. P.; Lin, J.; Siris, R.; Stimpel-Lindner, T.; Burke, K. F.; Mirabelli, G.; et al. Quantum Confinement-Induced Semimetal-to-Semiconductor Evolution in Large-Area Ultra-Thin PtSe$_2$ Films Grown at 400 °C. *npj 2D Mater. Appl.* **2019**, *3*, 33.

(47) El Sachat, A.; Xiao, P.; Donadio, D.; Bonell, F.; Sledzinska, M.; Marty, A.; Vergnaud, C.; Boukari, H.; Jamet, M.; Arregui, G.; et al. Effect of Crystallinity and Thickness on Thermal Transport in Layered PtSe$_2$. *npj 2D Mater. Appl.* **2022**, *6*, 32−39.

(48) Mogili, N. V. V.; Verissimo, N. C.; Abeykoon, A. M. M.; Bozin, E. S.; Bettini, J.; Leite, E. R.; Souza Junior, J. B. Background Optimization of Powder Electron Diffraction for Implementation of the E-PDF Technique and Study of the Local Structure of Iron Oxide Nanocrystals. *Acta Crystallogr., Sect. A* **2023**, *79*, 412−426.

(49) Souza Junior, J. B.; Schleder, G. R.; Colombari, F. M.; de Farias, M. A.; Bettini, J.; van Heel, M.; Portugal, R. V.; Fazzio, A.; Leite, E. R. Pair Distribution Function from Electron Diffraction in Cryogenic Electron Microscopy: Revealing Glassy Water Structure. *J. Phys. Chem. Lett.* **2020**, *11*, 1564−1569.

(50) Souza Junior, J. B.; Schleder, G. R.; Bettini, J.; Nogueira, I. C.; Fazzio, A.; Leite, E. R. Pair Distribution Function Obtained from Electron Diffraction: An Advanced Real-Space Structural Characterization Tool. *Matter* **2021**, *4*, 441−460.

(51) Hao, R.; Feng, Q. L.; Wang, X. J.; Zhang, Y. C.; Li, K. S. Morphology-controlled growth of large-area PtSe2 films for enhanced hydrogen evolution reaction. *Rare Met.* **2022**, *41*, 1314−1322.

(52) Wang, Z.; Xiao, B.; Lin, Z.; Xu, Y.; Lin, Y.; Meng, F.; Zhang, Q.; Gu, L.; Fang, B.; Guo, S.; Zhong, W. PtSe$_2$/Pt Heterointerface with Reduced Coordination for Boosted Hydrogen Evolution Reaction. *Angew. Chem., Int. Ed.* **2021**, *60*, 23388−23393.

(53) Chia, X.; Adriano, A.; Lazar, P.; Sofer, Z.; Luxa, J.; Pumera, M. Layered Platinum Dichalcogenides (PtS$_2$, PtSe$_2$, and PtTe$_2$) Electrocatalysis: Monotonic Dependence on the Chalcogen Size. *Adv. Funct. Mater.* **2016**, *26*, 4306−4318.

(54) Ping, X.; Liang, D.; Wu, Y.; Yan, X.; Zhou, S.; Hu, D.; Pan, X.; Lu, P.; Jiao, L. Activating a Two-Dimensional PtSe$_2$ Basal Plane for the Hydrogen Evolution Reaction through the Simultaneous Generation of Atomic Vacancies and Pt Clusters. *Nano Lett.* **2021**, *21*, 3857−3863.

(55) Cho, Y. S.; Rhee, D.; Lee, J.; Jung, S. Y.; Eom, J.; Mazanek, V.; Wu, B.; Kang, T.; Baek, S.; Choi, H.; Sofer, Z.; Lee, S.; Kang, J. Electronic and electrocatalytic applications based on solution-processed two-dimensional platinum diselenide with thickness-dependent electronic properties. *EcoMat* **2023**, *5* (8), No. e12358.

(56) Shanmugam, J.; Borisenko, K. B.; Chou, Y. J.; Kirkland, A. I. ERDF Analyser: An Interactive GUI for Electron Reduced Density Function Analysis. *SoftwareX* **2017**, *6*, 185−192.

(57) Proffen, T.; Neder, R. B. DISCUS: A Program for Diffuse Scattering and Defect-Structure Simulation. *J. Appl. Crystallogr.* **1997**, *30*, 171−175.

(58) Neder, R. B.; Proffen, T. Exact and Fast Calculation of the X-Ray Pair Distribution Function. *J. Appl. Crystallogr.* **2020**, *53*, 710−721.